Broadband Powerline Communication for Low-Voltage Microgrids

Derek C. Neal, *Member, IEEE*, Dan J. Rogers, Senior *Member, IEEE*

***Abstract*—The distributed-element transmission line model is modified to account for proximity effects in multiconductor cables and frequency dependent dielectric behaviour providing an accurate prediction of channel attenuation at broadband power line communication frequencies (1-100 MHz). The modified model is verified with scattering parameter measurements and then used as a building block for complex microgrid network modelling. Powerline communication performance tests are conducted using the HomePlug GreenPHY and HomePlug AV. The AV operates successfully up to 600 m on star feeders and on complex radial feeders in the presence of power converter noise. The GreenPHY operates up to 450 m on star feeders and on radial feeders with long branches. However, it cannot connect reliably on radial feeders with short branches due to frequency selective notching. Functionality requires link attenuation less than -60 dB at 30 MHz and the absence of notches that penetrate below -70 dB within the band (1.8-30 MHz). Due to the wide availability and low cost of the AV, it is a sensible choice for reliable broadband digital communications on microgrid networks.**

***Index Terms*—transmission line model, HomePlug, microgrid, powerline communication, scattering parameters, smart grid**

Nomenclature

ABL	adaptive bit loading
AMI	automatic metering infrastructure
AV	HomePlug AV
BB	broadband powerline communication
DUT	device under test
EMI	electromagnetic interference
GP	HomePlug GreenPHY
NB	narrowband powerline communication
OFDM	orthogonal frequency division multiplexing
PLC	powerline communication
QAM	quadrature amplitude modulation
QPSK	quadrature phase shift keying
SNR	signal-to-noise ratio
SWA	steel wire armour
TLM	transmission line model
UNB	ultra-narrow band powerline communication
VNA	vector network analyser
δ	skin depth of copper conductor
ε_r	relative permittivity of dielectric
ε	permittivity of dielectric ($\varepsilon_0\varepsilon_r$)
f	frequency in Hertz (Hz)
γ	propagation constant
Γ	reflection coefficient
$\tan\delta$	loss tangent of dielectric
μ	permeability of conductor
μ_0	permeability of free space
μ_r	relative permeability of conductor
σ	conductivity of conductor
T	transmission coefficient
z	cable length
Z_0	characteristic impedance

I. Introduction

POWERLINES are designed for the transmission of power rather than information and therefore offer a challenging environment for digital communications. In addition to the standard challenges inherent to any communication medium (e.g. attenuation, dispersion, distortion), powerline cables typically have non-homogeneous dielectrics and present non-standard characteristic impedances that cause frequency-dependent reflections. Powerline networks are difficult to model due to their often complex branching structures and because generators and loads may connect and disconnect, changing the electrical behaviour of the network over time. Generators, power converters, and dynamic loads inject broad- and narrow-band noise into the powerline. Ambient noise from nearby radio-electric systems can cause further electromagnetic interference (EMI). Therefore, powerlines are highly variable communication channels, and so channel models must depend on transmission band, cable type, network configuration, and load characterization.

Three frequency ranges are commonly used for Powerline Communication (PLC): ultra-narrow band (UNB: <3 kHz), narrowband (NB: 3-500 kHz), and broadband (BB: >1 MHz) [1]. UNB does not suffer as much from the aforementioned problems due to long wavelengths and minimal attenuations making low data rate single carrier transmissions a possible option for many applications. Lumped element models are sufficient for most UNB analysis [2]. Power utility companies are now using NB multicarrier orthogonal frequency division multiplexing (OFDM) modulation protocols like G3 and Prime to enable Automatic Metering Infrastructure (AMI) [3]. G3 and Prime use similar technology to BB PLC protocols like HomePlug which was primarily developed for indoor internet access via building electric wiring [4].

Following the HomePlug Alliance initial standards release in 2001, there has been a steady interest in PLC modelling and implementation in a variety of BB applications. Much of the first wave of interest concerned internet access whereas

This work is supported in part by the UK Engineering and Physical Sciences Research Council under Grant No: EP/R030111/1.

The authors are with the Power Electronics Group, Department of Engineering Science, University of Oxford, Oxford OX1 3PA, U.K. (e-mail: derek.neal@eng.ox.ac.uk; dan.rogers@eng.ox.ac.uk)

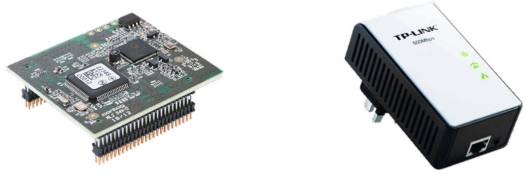

a) b)

Fig. 1. HomePlug PLC devices. a) dLAN Green PHY module b) TP Link AV500.

more recent research mainly concentrates on smart grid applications [1]. This study will focus on comparing the HomePlug Green PHY (GP) and HomePlug AV (AV), two BB off-the-shelf products (Fig. 1), as low-cost plug-and-play solutions for microgrid developers. We show that despite the GP's intention to be a tailored solution for smart grid applications, it cannot compete with the performance, availability, and affordability of the AV technology.

As isolated power systems, microgrids provide a natural canvas to implement the concepts of the smart grid. Therefore, using hardware from a low voltage microgrid designed for an electrification initiative in rural Kenya [5], the GP and AV are tested for their suitability for smart grid applications. The main contribution of this paper is to empirically evaluate the viability of these two BB PLC technologies for digital communications on a low voltage microgrid. Although the concepts presented hereafter may be applicable to larger grids, the stated results are limited to single common distribution voltage grids. Any voltage conversion would likely require repeaters. A network model will be presented as a tool for microgrid developers to determine if a particular powerline configuration will be conducive to BB PLC functionality.

Section II summarizes the status of PLC in the literature. Section III summarizes the transmission line distributed element model (TLM) that forms the foundation of the proposed network model. Section IV explains the model for the PLC analogue coupling circuit. Section V describes the PLC experimental setup used to evaluate PLC performance and Section VI follows with the test results.

II. Literature Review

PLC promises digital communication over a 'free medium', much like wireless technologies, whilst also potentially offering the reliability and high bandwidths of a wired communication technology. BB PLC technologies (e.g. HomePlug, G.hn) rose with the societal dependence on internet in the mid-2000s and was heavily explored as an access solution to compete with other 'last mile' wired technologies (e.g. DSL, coax, fibre) [6]. Although PLC did not rise as a leading solution, the HomePlug AV technology has had great success as an indoor internet extender in situations where other technologies fail to satisfy network requirements. Consequently, AV hardware can be found all over the world at affordable prices. Recently, PLC solutions have also remerged as a potential solution for the smart grid, meaning the connectivity of power systems for distribution automation, advanced metering infrastructure (AMI), demand side management (DSM), distributed power electronics control, energy management, and data harvesting [7]. Most smart grid applications only require NB capabilities with bit rates less than 1 kbps and latencies less than 100 ms [8]. However, the availability and ready-to-use nature of the AV makes it an attractive and low-cost solution for microgrid communication. Additionally, as the number of sensors, sample frequencies, and controllable devices increase, BB bit rates become necessary. Furthermore, many smart grid structures aspire to integrate all devices into cloud-based, internet-accessible control centres and BB communication solutions are typically based on Internet Protocol (IP) and so readily enable this capability [9].

This study was prompted specifically by the HomePlug GreenPHY (GP), a BB PLC technology designed as a robust low-power alternative to its higher-bandwidth relative the HomePlug AV (AV), for smart grid applications such as electric vehicle (EV) charging networks [10]. They both use OFDM techniques in the frequencies between 1-30 MHz. The basic AV offers data rates up to 200 Mbps using 1024-quadrature amplitude modulation (QAM) [11]. Later generations stretch the spectrum up to 86 MHz to achieve rates up to 1 Gbps. The TP Link AV500 model in Fig. 1b used in this study achieves data rates of over 300 Mbps using carriers up to 68 MHz. AVs use adaptive bit loading (ABL), varying the payload on each carrier to unload those that are severely attenuated while loading strong carriers. The GP does not utilize ABL, is limited to quadrature phase shift keying (QPSK) and so offers data rates up to 10 Mbps. Upon release, the GP was marketed as a cheaper and simpler AV that uses less energy. Modules using GP also include additional features to comply with the SAE J1772 EV charging standard [10].

Most PLC research focuses on modelling the harsh powerline communication medium to best predict performance. Methods fall into two main categories: top-down models based on measurements of the channel, and bottom-up models based on analytical characterisation of the channel using the transmission line model (TLM) [12]. Top-down models consider the communication network as a black box characterized as a transfer function derived from measurements in and out of the box [13],[14]. Such transfer functions contain two primary terms: attenuation and delay [15],[16]. Conversely, bottom-up models are built by defining each element of the network by its physical geometry and cascading those elements together with multiport mathematical matrices (e.g. s-parameters, ABCD) [17]. Time variance due to dynamic loads and noise can be added to either model [18]. Statistical analysis and method combinations can generate random channel predictions [19],[20]. Ultimately, the top-down method requires physical access to the channel for measurements. The bottom-up method is used by this study to offer microgrid developers a pre-design prediction of performance to inform the communication system choice. Some network topologies are problematic for PLC and require configuration modification or repeaters. PLC may not be the optimal engineering choice in these situations.

PLC must overcome three main obstacles: impedance mismatch, frequency selective attenuation, and noise. All these obstacles can either be permanent phenomena due to the grid structure or vary in time due to dynamic loads, charging cycles, EMI, and transients (e.g. contactor operation, lightning). Noise sources can be native to the network (e.g. power converters, loads) or interference from external equipment (e.g. EMI) [21]. AV and GP use differential coupling which reduces these effects [22]. Performance depends on feeder length and grid topology (e.g. star, radial). BB PLC systems are naturally limited to link lengths of a few hundred meters due to the high frequency attenuation of power cables. Some carriers may be attenuated further if the feeder length equals a multiple of the carrier's quarter wavelength. Branches on radial feeders cause multipath reflections resulting in deep attenuation notches in the frequency response and delay spread [23].

An inverter-based low voltage DC microgrid is described in [24] that uses first-generation HomePlug modems for communication across buried 4-core cable. Different cable types and combinations of differential signalling are tested. The effect of power converter and cable termination impedances are investigated. Propagation modes using the shield do not perform as well as interior cores. They propose dedicated interior cores on star feeders to achieve up to 500 m transmission. Cascaded s-parameters are used to simulate branched medium voltage radial feeders in [25] and they compare cumulative capacity (in Mbps) to overhead lines. The researchers conclude that overhead lines tend to be more conducive to PLC due to their separation, but buried cables allow higher injection power and help suppress noise, which can increase performance. They also observe that short branches (< 50 m) impair the channel response more than long branches due to quarter wave resonance. Various studies evaluate HomePlug performance variables. However, the literature lacks a methodical quantification of performance as a function of cable length and branch position and length in the presence of power electronic noise in a live microgrid. This quantification looks primarily at channel attenuation and notch depth as a means of determining functionality.

Researchers in [26] build complex PLC networks using ns-3, a software tool primarily used by wireless IP-based network simulation. Similarly, in [27], networks are made using EMTP-ATP, a power grid transient simulator. While both offer a GUI and employ the same fundamental TLM, they are difficult to access, overly complex, and not validated by experimental data.

Alternatively, this study synthesizes the PLC modelling literature to suggest a simple user-friendly modified two-wire cascaded s-parameter-based network building tool. The tool can be used as input into any software. Here the RLGC building block in the user-friendly AWR Microwave Office (by Cadence) GUI is used to quickly build complex networks and predict BB PLC performance. This tool is designed specifically for s-parameter analysis and is fast and easy to use. MATLAB and SIMULINK also have a RLGC block. These software tools all uses the same TLM and can be used to approximate the performance of a differential PLC signal on any two conductors in a multiconductor cable. The model is validated by vector network analyser (VNA) measurements of a testbed microgrid.

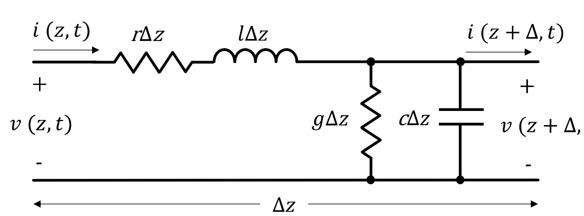

Fig. 2. Distributed element model of two-wire transmission line where Δz is an infinitely small length of cable and voltage and current behave like propagating waves. Reproduced from [2].

III. Modified Two Wire Transmission Line Model

As the signal wavelength becomes less than ten times the cable length, the channel must be modelled as a distributed element transmission line to account for wave propagation behaviour [2]. The distributed element TLM in Fig. 22 considers an infinitely small section of cable with two conductors where z is length of the line. The transmission line conductor is modelled with a series resistance and shunt admittance that cause frequency dependent signal attenuation. Series inductance and shunt capacitance affect signal propagation. Per-unit parameters can be mathematically derived from the cable cross sectional dimensions and material composition as in Fig. 33. Geometric variables are defined in an example 1.5 mm^2 Steel Wired Armour (SWA) cable in Fig. 3b. Frequency dependence of the ac resistance is considered when the radius of the conductor is greater than twice the skin depth as defined in [2]:

$$\delta(f) = \frac{1}{\sqrt{\pi f \mu \sigma}}\,[\mathrm{m}] \tag{1}$$

where f is frequency in Hertz, and $\mu = \mu_0\mu_r$. The two-wire AC per unit resistance is calculated with (2) using geometric terms from Fig. 3. It accounts for proximity effects of the two cores and the surrounding shield from multiconductor cable analysis [28]. Two-wire models built into software tools neglect proximity effects causing underestimations of high frequency attenuation for buried cables. Eq. (2) assumes a differential PLC signal across the two primary cores. Other propagation modes are not explored since previous studies show them to perform worse than interior cores. This multiconductor equation is necessary to accurately predict high frequency attenuation which is important when attempting to understand the behaviour of broadband PLC systems (e.g. AV2 which operates up to 86 MHz):

$$r(f) = \frac{2}{\pi r_{\mathrm{w}} \sigma \delta(f)}\left(1 + \frac{1+2\left(\frac{d}{r_{\mathrm{w}}}\right)^2}{4\left(\frac{d}{r_{\mathrm{w}}}\right)^4}\left(1 - 4\left(\frac{w}{2r_{\mathrm{s}}}\right)^2\right)\right)\left[\frac{\Omega}{\mathrm{m}}\right] \tag{2}$$

Measurable inductance is the sum of external inductance and internal inductance as in (3). The internal inductance (4) is frequency dependent where the external inductance (5) is a constant.

$$l = l_{\mathrm{ext}} + l_{\mathrm{int}}\left[\frac{\mathrm{H}}{\mathrm{m}}\right] \tag{3}$$

$$l_{\mathrm{int}} = \frac{1}{4\pi r_{\mathrm{w}}}\sqrt{\frac{\mu}{\pi f \sigma}}\left[\frac{\mathrm{H}}{\mathrm{m}}\right] \tag{4}$$

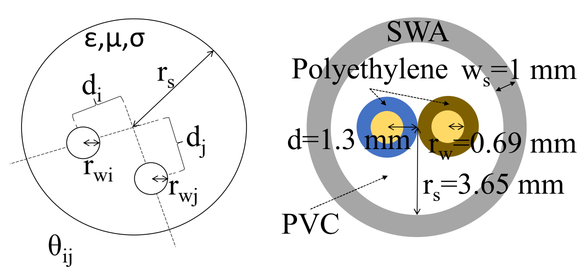

a) b)

Fig. 3. Cross sectional geometry of a) generic shielded multiconductor cable b) 1.5 mm^2 SWA 2-core power cable

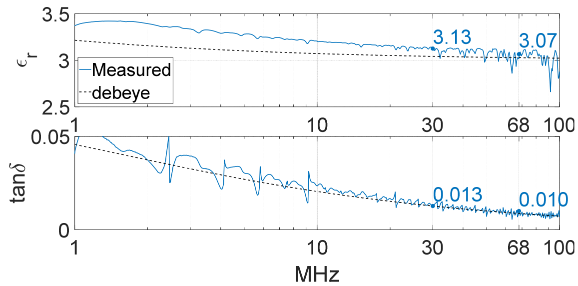

Fig. 4. Measured dielectric properties of 1.5 mm² SWA power cable vs the Debye approximation.

$$l_{\text{ext}} = \frac{\mu}{\pi}\cosh^{-1}\left(\frac{d}{r_{\text{w}}}\right)\ \left[\frac{\text{H}}{\text{m}}\right] \tag{5}$$

Capacitance and admittance are defined by (6) and (7) and assume a homogeneous dielectric insulation:

$$c(f) = \frac{\pi\varepsilon(f)}{\cosh^{-1}\left(\frac{d}{r_{\text{w}}}\right)}\ \left[\frac{\text{F}}{\text{m}}\right] \tag{6}$$

$$g(f) = 2\pi f c(f)\tan\delta(f)\ \left[\frac{\text{S}}{\text{m}}\right] \tag{7}$$

Both the relative permittivity (ε_r) and the loss tangent ($\tan\delta$) decrease with frequency and are intrinsic to the insulation material [29]. To accurately predict attenuation at high frequency, dielectric constants must be chosen carefully to best predict PLC attenuation at the envelops of operation. The model must utilize a frequency dependent function or choose a constant value that is accurate in the upper band.

The frequency dependence of the dielectric can be represented using the Debeye function with the Cole-Cole modification as in [30],[31]:

$$\varepsilon_{\text{r}}(\omega) = \varepsilon'_{\text{r}}(\omega) - j\varepsilon''_{\text{r}}(\omega) = \varepsilon_\infty + \frac{\varepsilon_0 - \varepsilon_\infty}{1+(j\omega\tau)^{\varphi}} \tag{8}$$

$$\tan\delta = \frac{\varepsilon''_{\text{r}}}{\varepsilon'_r} \tag{9}$$

where ε_0 is the value at DC, ε_∞ is the settling value at high frequency, τ is the dielectric relaxation time constant which defines the frequency around which the dielectric constant relaxes to a different value, and φ is a stretching factor determining the width of frequency range over which the relaxation occurs.

Values for ε_0 and ε_∞ are best observed from measurement but can be estimated from look up charts for dielectric materials [32],[33]. The following solution is extracted from curve fitting the Debye equation to s-parameter measurements and serves as the model of the dielectric of the 1.5 mm² SWA test cable from Fig. 33b. It is compared to the measurement in Fig.4.

$$\varepsilon_r(\omega) = 3 + \frac{4-3}{1+(j\omega 1.5\times10^{-6})^{0.5}}$$

Circuit analysis of Fig. 22, assuming steady state conditions in the time domain, yields the characteristic impedance (Z_0) in (10) defined as the ratio of voltage to current for a traveling wave on a transmission line and is calculated using the per-unit values previously defined.

$$Z_0 = \frac{V^+}{I^+} = \frac{-V^-}{I^-} = \sqrt{\frac{r+j\omega l}{g+j\omega c}}\ [\Omega] \tag{10}$$

The propagation constant γ in (11) is also calculated from the per-unit values and consists of α (nepers/m), the attenuation constant that describes the decay of the signal, and β (radians/m), the phase constant that expresses the amount of phase change per unit length of transmission line or, in other words, how fast the signal's phase varies as it moves along the line [2].

$$\gamma = \alpha + j\beta = \sqrt{(r+j\omega l)(g+j\omega c)}\ [\text{m}^{-1}] \tag{11}$$

These two values (Z_0 and γ) characterise a transmission line and form the foundation of the two-wire TLM.

After taking open and short s-parameter measurements as in [34], the characteristic impedance and propagation constant (Z_0 & γ) can then be derived from (12)-(13) and thereafter each of the per-unit parameters in (14)-(17).

$$Z_0 = \sqrt{Z_{\text{in\_sc}} Z_{\text{in\_oc}}} \tag{12}$$

$$\gamma = \frac{1}{l_{\text{cable}}}\operatorname{atanh}\sqrt{\frac{Z_{\text{in\_sc}}}{Z_{\text{in\_oc}}}} \tag{13}$$

$$r = \text{Re}\{\gamma Z_0\} \tag{14}$$

$$l = \frac{1}{2\pi f}\text{Im}\{\gamma Z_0\} \tag{15}$$

$$g = \text{Re}\left\{\frac{\gamma}{Z_0}\right\} \tag{16}$$

$$c = \frac{1}{2\pi f}\text{Im}\left\{\frac{\gamma}{Z_0}\right\} \tag{17}$$

where l_{cable} is the length of the cable. Open/short measurements of a 50 m section of SWA cable yields Fig. 5.

The phase velocity for this cable relates to the conductivity of the copper conductor and the permittivity of the dielectric as in (18).

$$v_{\text{p}} = \frac{2\pi f}{\beta} = \frac{c}{\sqrt{\mu_{\text{r}} e_{\text{r}}}} \tag{18}$$

$$\lambda = \frac{v_{\text{p}}}{2\pi f} \tag{19}$$

where c is the speed of light. Phase velocity for the SWA cable is approximately $1.65 \times 10^8\,\frac{\text{m}}{\text{s}}$; therefore, a 50 m line will have its first quarter-wave resonance at ~80 kHz as

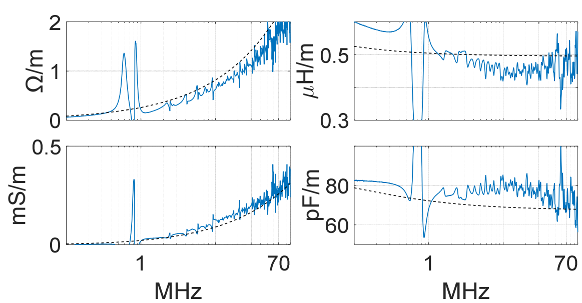

a)

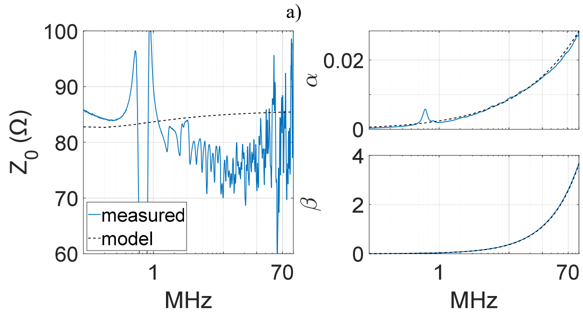

b)

Fig. 5. Measured per unit parameters as compared to the two-wire TLM distributed element model for 1.5 mm² SWA power cable a) RLGC b) characteristic impedance and propagation constant.

notable in the first oscillation in Fig. 5. To avoid reflections and the oscillatory nature of the measurements, the device under test (DUT) would need to be shorter than the quarter wavelength (1.4 m @ 30 MHz). However, the smaller the DUT, the more accentuated measurement errors become and, although the curves look smoother, they are not as accurate.

IV. Powerline Coupling Circuit

Full path measurements are taken looking through the PLC analogue front end (AFE) coupling circuit modelled in Fig. 6 found on the GP evaluation board made by devolo and purchased from Codico [35],[36]. It includes a three-winding transformer (devolo UT11359) to step up the PLC signal both upon transmission and reception [37]. The transformer is modelled as an ideal three-coil mutually coupled inductor [38]. Leakage inductance is modelled as an additional inductor placed in series with the transmit coil per the transformer data sheet [37]. Coil 1 is the receiver, coil 2 the transmitter, and coil 3 connects to the impedance matching resistor of 96 Ω before connecting to the powerline (close to the cable's characteristic impedance seen in Fig. 5b). In parallel with the transformer is a capacitive low pass filter to block frequencies above the band of interest (1-30 MHz).

The AFE model was made in AWR because of the user-friendly GUI designed for rapid 2-port network design and s-parameter graphical analysis. Fig. 7 shows the transmission coefficient S21 looking through the transmitter AFE through 10 cm of coaxial cable directly to the receiver AFE. The bandpass shape of the AFE response is deliberate to reject both switching noise below the PLC bandwidth and any communication signals above the band. This shape will dominate the network VNA measurements.

The s-parameters for an ideal transformer in the passband is determined by (20):

$$S_{\mathrm{xfr}}(n) = \frac{1}{n^2+1}\begin{bmatrix} n^2-1 & 2n \\ 2n & 1-n^2 \end{bmatrix} \text{[dB]} \qquad (20)$$

where n is the number of turns [39]. The GP transformer has a 1:4:5 (TX:powerline:RX) ratio and therefore $n = 5$ from transmit to receive.

$$S_{\mathrm{tx}}(5) = \begin{bmatrix} -0.7 & -8.3 \\ -8.3 & -0.7 \end{bmatrix} \text{[dB]}$$

Fig. 7 shows the 8.3 dB S21 attenuation from the transformer plus approximately 2 dB more from the matching resistor network.

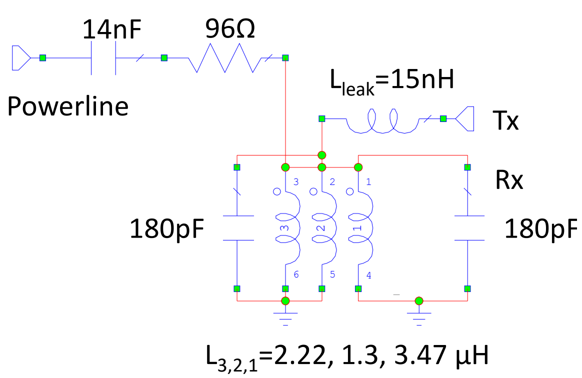

Fig. 6. Model of HomePlug GP coupling transmitter circuit modelled in Cadence AWR Microwave Office software. Tx/Rx nodes connect to the respective Tx/Rx pins of the QCA7000 PLC modem.

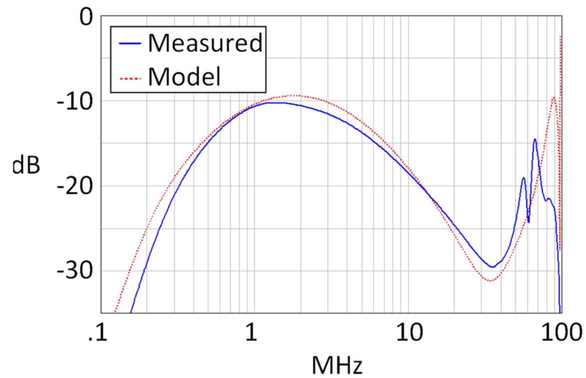

Fig. 7. S21 from GP transmitter connected to a GP receiver with a 10 cm coaxial cable showing the effect of the coupling transformer circuits.

V. Test Setup

The HomePlug products are tested on a lab-based 120V DC microgrid intended for a remote rural community [5]. The experimental setup in Fig. 8 is used to evaluate PLC performance on a given cable network. In this test, microgrid power flows from a generator to a load via power electronic converters. Those converters are mostly capacitive in nature and present a low impedance path for PLC frequencies. Therefore, low pass filters (LPF), placed between the converters and the powerline, are necessary to present a high impedance to PLC signals. The network consists of various lengths and branching configurations of SWA power cable, represented with a TLM circuit diagram. Feeders range between 50 – 800 m. Branches are either short (< 50 m) or long (> 50 m).

Internet Protocol (IP) test data originates at the Linux computer. The data is addressed to a *namespace*, a self-contained partition to tunnel data through a USB-ethernet adapter forcing communication down the powerline vs internally in the Linux machine. The PLC modem modulates the signal and transmits a differential voltage OFDM symbol that is then coupled to the powerline through the AFE coupling filter discussed in the previous section. The signal is received by another PLC modem at the opposing node, demodulated, and passed to the receiving Linux namepace IP address.

VNA measurements taken at the 'X' test points measure just the network of powerlines versus measurements behind the AFE at the circle test points observe the full PLC signal path (as in Fig. 7).

Two software utilities are used to generate internet IP test data on the Linux machine. `Ping` measures network latency by measuring roundtrip time for an IP message to travel from transmitter to receiver and back. The Linux processing

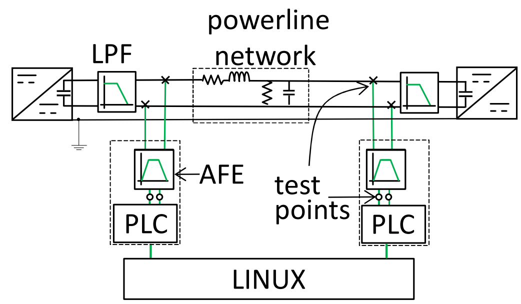

Fig. 8. Network performance test setup.

contributes 0.4 ms. The powerlines contribute (based on approximately $1.65 \times 10^8 \frac{\text{m}}{\text{s}}$ transmission speed) less than 0.003 ms. Any remaining latency is due to the PLC modem pair. When a reliable PLC connection is established, latencies are consistently around 10 ms for the GP and 4 ms for the AV. These numbers do not vary with network structure since the modulation techniques operate to guarantee latency consistency.

`Iperf` similarly produces a stream of IP data from client (transmitter) to server (receiver) at channel max capacity to measure throughput, jitter, and packet loss or retries. Jitter is latency deviation and tends to rise with channel degradation. Although this is not a particularly reliable indicator. Data can be packaged in transmission control protocol (TCP) or user datagram protocol (UDP) format. The main difference is TCP's need for a transmission receipt. When the client does not receive a receipt from the server, the client retries. UDP, on the other hand, transmits indiscriminately which can lead to packet loss. HomePlug modulation techniques also sacrifice throughput to maintain acceptable thresholds of packet loss and retries. That leaves throughput as the main variable to evaluate PLC performance. There is a clear relationship between throughput and channel quality as will be demonstrated shortly.

In addition to the Linux utilities, the HomePlug modems made by Qualcomm Atheros (QCA) have software tools called the Open Powerline Toolkit that can be used to evaluate performance. These tools are open source [40]. Each modem chip has a unique MAC address which is used to interrogate the chip for various parameters. Three commands were used in the PLC tests:

1. `int6k`: interrogates the modem and prints the network configuration. It identifies which chip address has established itself as Central Coordinator (CCo) and which are its subordinate stations [10]. Any chip can act as either. The program is used to quickly assess if two or more modems have established a network.
2. `plctone`: prints signal-to-noise ratio (SNR) tone map. The chip exchanges investigative packets with network neighbours to assess the channel quality to create a tone map as in Fig. 9. The tone map also incorporates pre-masked carriers and is then used for ABL protocols. This feature only works on the AV chip.
3. `plcrate`: polls all modems on the network and prints physical data rates in bits per second (bps). This is the maximum transmission rate capability of the modem for a given tone map. This feature only works on the AV chip.

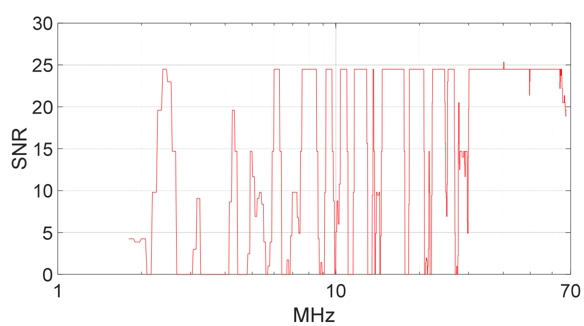

Fig. 9. HomePlug AV unitless SNR quantifier map on 50 m SWA cable.

Data rate is only based on the physical layer and establishes the ceiling capability whereas throughput is the actual bit rate achieved after software and hardware overhead. Throughput calculated by `iperf` will always be lower than the data rate reported by `plcrate`.

VI. PLC Performance on Microgrid networks

Microgrid power network architectures follow one of two basic structures: star or radial. Star feeders are direct and dedicated connections from a central generation bus to a load. Radial feeders consist of a main cable with several ancillary branches. Even though radial feeders must be larger to support higher currents, radial networks tend to use less cable, often making them cheaper and more common. BB PLC modulation techniques were originally designed for complex radial indoor networks with random lengths and multiple branches.

There are three main causes of attenuation that impede PLC connectivity: cable length, noise, and notches from branches and impedance discontinuities.

A. Star Feeders

The s-parameter transmission coefficient S21 shown in Fig. 10 (measured at the 'X' test points from Fig. 8) indicates attenuation solely due to cable length. Mixed-mode differential S21 VNA measurements in blue are compared to AWR model curves in red [41]. The AWR model consists of an RLGC element defined by Eqs. (2-7). The published reach of HomePlug products is 300 m; however, the GP can function up to 700 m and the AV up to 800 m on star feeders when microgrid power is off. Functionality decreases when microgrid power is turned on due to converter noise on the feeder. Measurements (in blue) become unreliable below -80 dB due to the VNA noise floor [42]. The threshold for GP operation on live star feeders is -60 dB of attenuation from the power cable at 30 MHz assuming factory average transmit power settings, measured at approximately 76mW. This equates to 450 m and a coherence bandwidth of 200 kHz at a correlation level of 0.7 [43].

The GP functionality limit is further illustrated in Fig. 11 that presents the fast Fourier transform (FFT) of full signal path time domain oscilloscope measurements (taken at the circle test points from Fig. 8). The scope shows received GP TCP messages over 50 m and 500 m star feeders. The frequency plot includes the noise associated with a dead network (microgrid power off in red) compared to a live feeder (microgrid power on in purple). There is an increase in the overall noise floor with distinct harmonic spikes in the

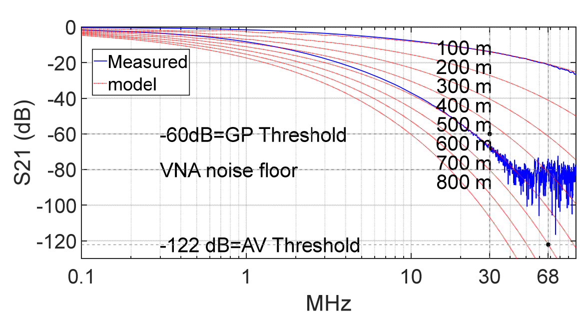

Fig. 10. S21 vs. cable length. VNA measurements (in blue) become unreliable at -80 dB. Lines are marked to show the limit of functionality on a live star feeder. The GP requires cable attenuation > -60 dB @ 30 MHz to establish reliable connectivity corresponding to a 450 m 1.5 mm² SWA cable star feeder. For the AV, cable attenuation > -122 dB @ 68MHz corresponding to 600 m.

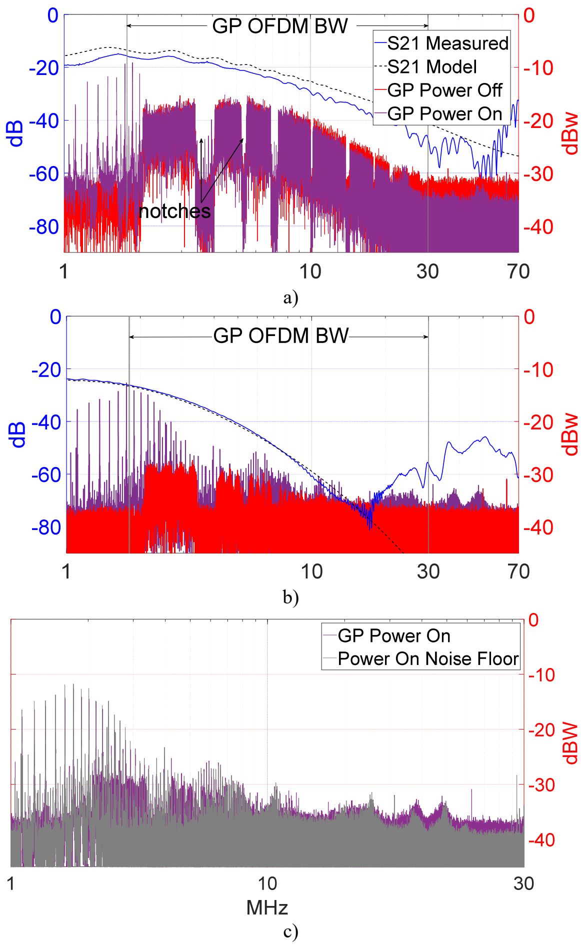

Fig. 11. FFT of oscilloscope measurements of received GP TCP OFDM symbols on a) 50 m and b) 500 m of SWA cable star feeder. Red shows reception with a dead cable (microgrid power off) while purple shows reception with a live feeder (microgrid power on) with the associated converter noise on the line. The FFT is compared to the S21 measurement and model of the same length. The FFT shows the OFDM symbol between 1.8-30 MHz tapering with the attenuation of the line as expected from the S21 curve. c) Zoom-in of the received GP TCP message at 500 m (in purple) compared to microgrid power on noise floor (in grey). Harmonic spikes debilitate the message making connection on the GP unreliable at 500 m on a live network.

lower frequencies caused by the switching power converters. Amongst the noise in Fig. 11 are clear PLC subcarrier groupings in the band between 1.8-30 MHz from the GP OFDM symbol. Pre-programmed notches are also visible. Since the GP does not use ABL, transmission power is the same at all frequencies; therefore, the amplitude of each received carrier suffers frequency dependent attenuation caused by the length of the star feeder. Hence, the OFDM symbol follows the shape of S21. Performance at 500 m is unreliable when power is flowing because the received power of the OFDM is exceeded by the noise as shown in Fig. 11c.

Since the GP does not use ABL, it relies on the ROBO technique of sending multiple copies of each data packet. To maximize the GP reach during performance tests, the ROBO setting is programmed at the most conservative level which sends five repeat copies of each packet [10]. With this setting, the GP data PHY rates are limited to 3.8 Mbps and throughputs of approximately 1.5 Mbps. These rates did not change with cable length or channel quality. There is no gradual decrease in performance. The GP either meets the connection threshold or it does not. Table I summarizes PLC functionality on star feeders for both the GP and AV when microgrid power is off or on.

In contrast to the GP, AV bit rate varies with channel quality. The relationship between cable length and data rate

TABLE I:
STAR FEEDER POWER-OFF & POWER-ON FUNCTIONALITY

	Cable length (m)					
	300	400	500	600	700	800
GP (power off)	✓	✓	✓	✓	✓	
GP (power on)	✓	✓				
AV (power off)	✓	✓	✓	✓	✓	✓
AV (power on)	✓	✓	✓	✓		

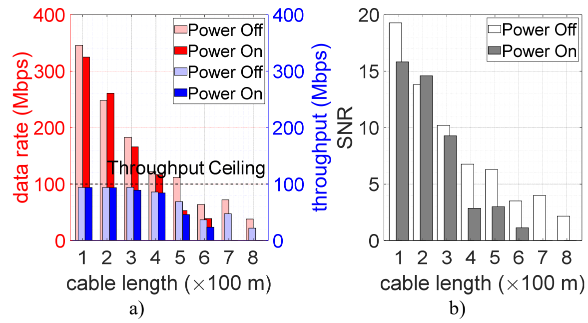

Fig. 12. Performance vs distance for the HomePlug AV. Light colours indicate microgrid power is off and dark colours show power is on. a) data rate and throughput vs. distance b) SNR vs. distance

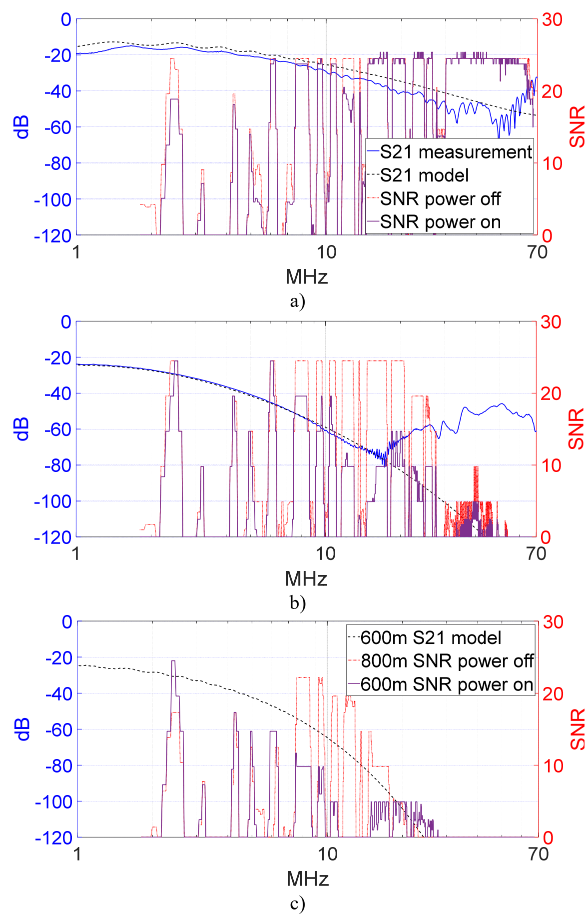

Fig. 13. SNR and to S21 on a) 50 m b) 500 m star feeder comparing the difference between microgrid power off (dotted red curve) and on (solid purple curve). At 50 m, noise has very little effect on subcarrier load whereas at 500 m, not only are higher frequency subcarriers attenuated by cable length, but higher frequencies are also more susceptible to microgrid power converter noise since operation is closer to the noise floor. c). A dead 800 m star feeder is compared to the AV reliable limit, a live 600 m.

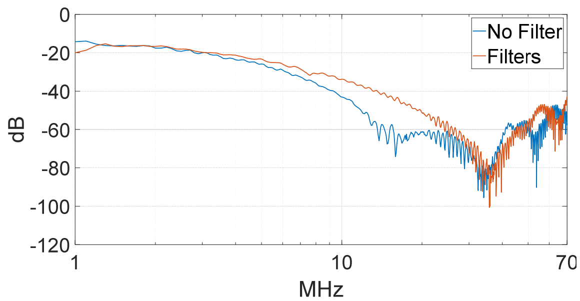

Fig. 14. S21 of 200m star feeder with and without inductive LPF in between load and PLC modem. The filters block capacitive loads and reduce attenuation throughout the PLC bandwidth.

is illustrated in Fig. 12a. Data rate (in red) is extracted using the QCA toolkit `plcrate` command whilst throughput (in blue) is measured using the `iperf` network performance utility. AV throughput is limited to 100 Mbps due to the RJ45 ethernet connectors used on the AV device (an odd engineering design choice). The mean SNR of the entire spectrum (1.8-68 MHz) in Fig. 12b is extracted from the QCA toolkit `plctone` command. From experimentation, it is determined that average SNR must be above 1.0 to achieve AV connectivity. Due to the hardware ceiling on AV throughput, data rate (`plcrate` command) and SNR (`plctone` command) reported by the QCA modem are the best predictors of channel performance.

From Fig. 12 and Table I, the AV functionality on a star feeder with microgrid power on is 600 m. Fig. 13 echoes this limitation showing how noise affects SNR at various cable lengths. SNR maps show the ABL in action and are compared to S21 (measured from circle test points from Fig. 8) looking through the GP AFE (under the assumption that the GP and AV AFE coupling circuits are very similar). At 50 m, converter noise does not affect SNR except for a small reduction in usage of the lower band subcarriers due to harmonic spikes. As cable length increases, the upper band is impaired due to signal attenuation where the noise has greater impact. With microgrid power on, the highest frequency of use on a 600 m live star feeder is 27 MHz and average SNR is 1.13 yielding a data rate capacity of 39 Mbps and throughput of 24 Mbps. ABL reduces data loads on higher frequencies. Although it is difficult to establish a fixed threshold definition for AV functionality due to the dynamic ABL, average SNR over the entire band must average above 1.0. Looking back at cable-only attenuation in Fig. 10, 600 m results in $S21 = -122$ dB at 68 MHz. Fig. 13 clearly demonstrates that at this distance, connectivity depends on the lower band subcarriers. Therefore, when S21 for a given network dips this low at 68 MHz, the network will be approaching its connectivity limit. AV average transmit power settings were measured at approximately 264 mW at these thresholds.

B. Radial Feeders

Branches on radial feeders cause multipath reflections and standing waves that create notches in the frequency response. The severity of the notches is determined by the branch length and branch termination. In this case, the branches terminate in a large LPF in front of a DC converter as in Fig. 8. Therefore, at PLC frequencies, the load termination appears as an open circuit which improves the frequency response as demonstrated in Fig. 14. The filter helps shield the PLC network from the problematic switching noise, load dynamics, and capacitive loading of the power converters.

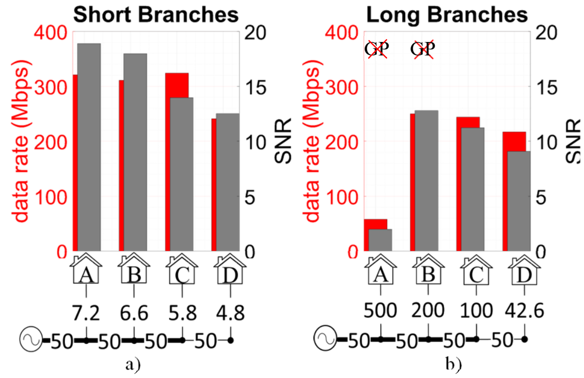

Fig.15. Experimental radial feeder networks with a) short branches and b) long branches labelled in meters. The PLC transmitter is placed at the microgrid hub indicated by a source. Receivers are placed at the end of each branch as designated by homes A-D. Cables represented by thick lines have SWA with 6 mm^2 cores while thin lines have SWA with 1.5 mm^2 cores. Data rates and SNR are reported by the AV and show good functionality on all branches. The GP also achieved connectivity on all branches except A and B of the long branch network due to cable length limitations.

Two radial test networks are shown in Fig. 15 that serve as the DUT for VNA and performance measurements using the same test setup from Fig 8. PLC signals are injected at the microgrid generation hub (indicated with a source in Fig. 15) and then received at one of the branch terminations (indicated with a lettered home). Each branch terminates at a power converter. Both the GP and AV establish connectivity at every load with two exceptions: the GP does not function on homes A and B on the long branch network. This is to be expected since A exceeds the GP cable length limit and B is very close to that limit. Comparisons of the S21 and SNR of houses D are reported in Fig. 16.

Branches that approach the length of the quarter wavelength of the PLC carriers cause resonant notches like the one seen at 7 MHz in Fig. 16a (in blue). Hence, shorter branches tend to be more problematic, especially for the GP.

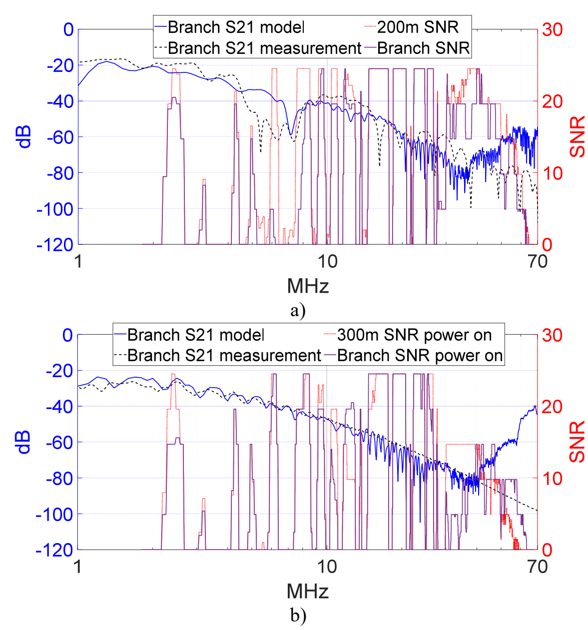

Fig. 16. SNR compared to S21 on a) Home 'D' of short branch network b) Home 'D' of long branch network. Branch SNR is compared the SNR for a comparable length of star feeder. Short branches create notches which are especially problematic for the GP that relies on all subcarriers. The branch lengths in the short network create a notch between 5-8 MHz and the AV reduces the data loading on those subcarriers. Long branches do not create deep notches.

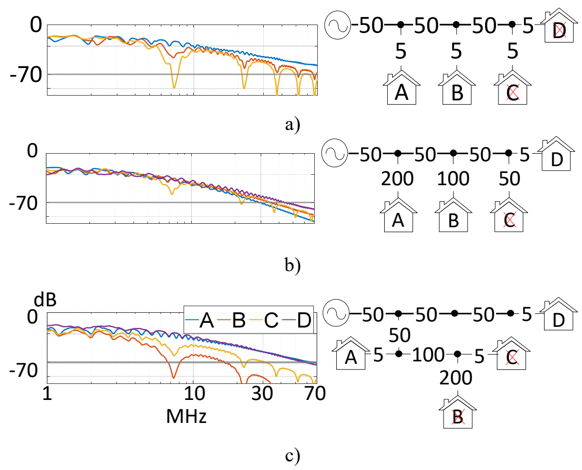

Fig. 17. S21 model estimates of three experimental radial feeder networks with a) short branches b) long branches and c) a complex network of branches extending from other branches of mixed lengths labelled in meters. Cables represented by thick lines have SWA with 6 mm^2 cores while thin lines have SWA with 1.5 mm^2 cores. Even with microgrid power on, the AV established connectivity at every home. The red X indicates that the GP failed to connect with microgrid power on. Such failures are due to notches that extend below -70 dB.

Note the AV ABL adjusts the subcarrier loading between 5-8 MHz due to this notch (purple vs. red). However, since the GP does not use ABL, it cannot reduce or eliminate the use of certain bands that may have deep notches. The notch in Fig. 16a only dips to -60 dB because the branches are of slightly different lengths and the GP still achieves connectivity. If the lengths of the branches become very similar in length, the notches grow in depth. The depth of the notch increases even more when two short branches extend from the same junction.

Three additional test networks in Fig. 17 illustrate this point. The AV establishes connectivity on every branch in each of the three networks. The lowest performing branch with microgrid power on is Fig. 17c Home B with SNR=0.5, data rate of 15 Mbps, and throughput of 5 Mbps. With microgrid power off, the GP established connection in all branches except the same mentioned above. But with microgrid power on, GPs on several branches failed to connect as indicated with a red X in Fig. 17. VNA measurements are not available for these test cases, but the model is used to approximate the channel. The models show deep notches that extend below -70 dB causing GP failure. These notches are most likely to occur in conjunction with either multiple short branches of similar length and/or due to a short branch hanging from the same junction as another branch.

One last test network in Fig. 18 helps define the threshold for the GP. When all the branches are connected, the GP cannot connect between the microgrid hub and Home A. The GP begins connecting after removing the three red branches. The GP sends and receives ping commands but is unable to transfer TCP or UDP data indicating the connection is not reliable. More branches would need to be removed for full functionality. The S21 measurements show the reduction in depth of two deep notches at 4 and 12 MHz. Both drop to -85 dB and are approximately 10 MHz wide. There are two other notches of similar severity at 6.2 and 7.4 MHz which do not improve after removing the three red branches. There are also many notches above 10 MHz, but since they are close to the VNA noise floor, it is difficult to conclude their characteristics and effect. At a correlation level of 0.7, measured coherence bandwidth is 206kHz (compared to 198kHz using the model) with all branches and 242 kHz with the red branches removed. From Fig. 16-Fig. 18 it is clear that the GP cannot make reliable connection in the presence of deep notches that extend below -70 dB.

VII. Conclusion

A bottom-up approach to network modelling yields a tool to predict PLC functionality on microgrids. An expanded two-wire distributed TLM forms the backbone of the model incorporating important proximity effects inherent to multiconductor cables and frequency dependent dielectric behaviour. S-parameter measurements validate the model and serve as the primary predictive tool for PLC functionality. Using the modified two-wire model as a building block, complex networks are built in AWR Microwave Office to rapidly produce S21 curves that predict PLC functionality for a given microgrid network structure.

Experimentation reveals the HomePlug AV has a star feeder reach of 600 m in the presence of power converter noise and performs well on complex branched networks due to ABL. Throughput bit rates exceed 10 Mbps even in the most extreme cases which surpasses communication requirements for microgrids [8]. Average SNR reported by the AV QCA must exceed 1 for connectivity which corresponds to a maximum cable-only attenuation of -122 dB at the highest used frequency, 68 MHz.

The GP also performs well on star feeders less than 450 m which equates to S21 power cable attenuation of -60 dB at 30 MHz. However, the GP struggles to make reliable connection on radial feeders with short branches due to frequency selective notching. Radial S21 curves must not contain notches in the PLC bandwidth (1.8-30 MHz) that dip below -70 dB.

Digital communication requirements for microgrids can be

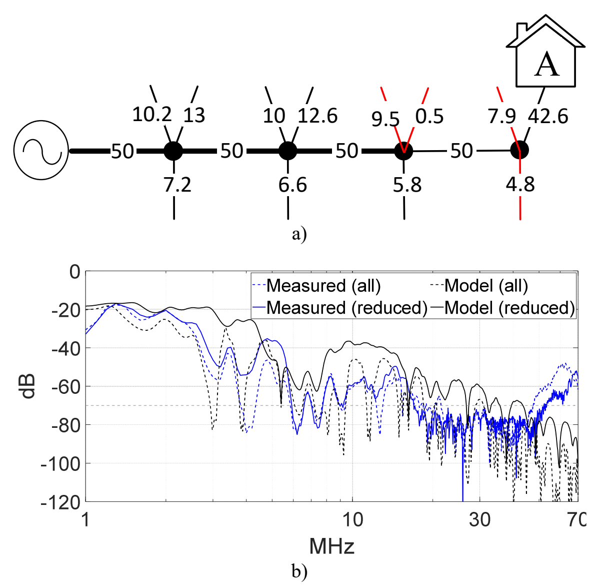

Fig. 18. a) Complex experimental radial feeder networks with several short branches labelled in meters. Cables represented by thick lines have SWA with 6 mm^2 cores while thin lines have SWA with 1.5 mm^2 cores. Red branches are removed to find GP functionality threshold. b) S21 measurements taken between the PLC source at the microgrid hub to Home 'A' of the complex radial feeder are compared to the model. Dotted lines show the network with all branches connected whilst solid lines show the network without the red branches. The GP begins connecting after removing the three red branches due to the shallowing of the deep notches at 4 and 12.7 MHz.

satisfied with HomePlug (or similar) devices after considering these limitations. The AV appears to be the superior choice due to its increased range and adaptability on radial feeders with various branch lengths. Additionally, the AV is an affordable and common product available all over the world as compared to the relatively obscure and still expensive GP.

Future work includes an investigation of the AV thresholds by extending the Fig. 18 experiment to ascertain the attenuation and coherence bandwidth differences between functionality and failure. Correlation levels should be fully explored to determine how flat the band needs to be for subcarrier utilization. Validation would require higher resolution high frequency VNA data and the incorporation of a noise model into the modified two-wire model.

VIII. References

[1] G. Lopez *et al*, "The Role of Power Line Communications in the Smart Grid Revisited: Applications, Challenges, and Research Initiatives," *Access,* vol. 7, pp. 117346-117368, 2019. Available: https://search.datacite.org/works/10.1109/access.2019.2928391. DOI: 10.1109/access.2019.2928391.

[2] C. R. Paul, *Analysis of Multiconductor Transmission Lines.* (2nd ed.) Hoboken, NJ: Wiley, 2008.

[3] *Narrowband orthogonal frequency division multiplexing power line communication transceivers for G3-PLC networks*, G.9903, ITU-T, 2017 [Online] Available: https://www.itu.int/rec/T-REC-G.9903

[4] S. Galli, A. Scaglione and Z. Wang, "For the Grid and Through the Grid: The Role of Power Line Communications in the Smart Grid," *Jproc,* vol. 99, *(6),* pp. 998-1027, 2011. Available: https://ieeexplore.ieee.org/document/5768099. DOI: 10.1109/JPROC.2011.2109670.

[5] D. Neal *et al*, "Demand side energy management and customer behavioral response in a rural islanded microgrid," in *IEEE PES/IAS PowerAfrica,* 2020.

[6] *Unified high-speed wireline-based home networking transceivers – System architecture and physical layer specification*, G.9960, ITU-T, 2017 [Online] Available: https://www.itu.int/ITU-T/recommendations/rec.aspx?rec=15555

[7] V. C. Gungor *et al*, "A Survey on Smart Grid Potential Applications and Communication Requirements," *IEEE Transactions on Industrial Informatics,* vol. 9, *(1),* pp. 28-42, 2013. Available: https://ieeexplore.ieee.org/abstract/document/6298960.

[8] D. Neal, "Powerline Communication and Demand Side Management for Microgrids." Ph.D. dissertation, Eng. Sci., Uni. of Oxford, Oxford, UK. 2023.

[9] T. Sauter and M. Lobashov, "End-to-End Communication Architecture for Smart Grids," *Tie,* vol. 58, *(4),* pp. 1218-1228, 2011. Available: https://ieeexplore.ieee.org/document/5559470. DOI: 10.1109/TIE.2010.2070771.

[10] HomePlug Powerline Alliance, "HomePlug green PHY: The standard for in-home smart grid powerline communications," HomePlug Powerline Alliance, Inc., Jun 14, 2010.

[11] HomePlug Powerline Alliance, "HomePlug AV white paper," HomePlug Powerline Alliance, Inc., 2005.

[12] C. Cano *et al*, "State of the Art in Power Line Communications: From the Applications to the Medium," *J-Sac,* vol. 34, *(7),* pp. 1935-1952, 2016. Available: https://ieeexplore.ieee.org/document/7467440. DOI: 10.1109/JSAC.2016.2566018.

[13] M. Zimmermann and K. Dostert, "A multipath model for the powerline channel," *Tcomm,* vol. 50, *(4),* pp. 553-559, 2002. Available: https://ieeexplore.ieee.org/document/996069. DOI: 10.1109/26.996069.

[14] R. Aquilue *et al*, "Scattering Parameters-Based Channel Characterization and Modeling for Underground Medium-Voltage Power-Line Communications," *Tpwrd,* vol. 24, *(3),* pp. 1122-1131, 2009. Available: https://ieeexplore.ieee.org/document/5109876. DOI: 10.1109/TPWRD.2008.2002963.

[15] H. C. Ferreira *et al*, *Power Line Communications.* 2010Available: http://ebooks.ciando.com/book/index.cfm/bok_id/496785. DOI: 10.1002/9780470661291.

[16] A. M. Tonello *et al*, "A Fitting Algorithm for Random Modeling the PLC Channel," *Tpwrd,* vol. 27, *(3),* pp. 1477-1484, 2012. Available: https://ieeexplore.ieee.org/document/6216470. DOI: 10.1109/TPWRD.2012.2196714.

[17] S. Galli and T. Banwell, "A novel approach to the modeling of the indoor power line channel-Part II: transfer function and its properties," *Tpwrd,* vol. 20, *(3),* pp. 1869-1878, 2005. Available: https://ieeexplore.ieee.org/document/1458855. DOI: 10.1109/TPWRD.2005.848732.

[18] S. Galli and T. C. Banwell, "A deterministic frequency-domain model for the indoor power line transfer function," *J-Sac,* vol. 24, *(7),* pp. 1304-1316, 2006. Available: https://ieeexplore.ieee.org/document/1650331. DOI: 10.1109/JSAC.2006.874428.

[19] A. M. Tonello and F. Versolatto, "Bottom-Up Statistical PLC Channel Modeling-Part I: Random Topology Model and Efficient Transfer Function Computation," *Tpwrd,* vol. 26, *(2),* pp. 891-898, 2011. Available: https://ieeexplore.ieee.org/document/5688213. DOI: 10.1109/TPWRD.2010.2096518.

[20] F. J. Canete *et al*, "A channel model proposal for indoor power line communications," *Com-M,* pp. 166-174, 2011. Available: https://ieeexplore.ieee.org/document/6094022. DOI: 10.1109/MCOM.2011.6094022.

[21] M. Gotz, M. Rapp and K. Dostert, "Power line channel characteristics and their effect on communication system design," *Com-M,* vol. 42, pp. 78-86, Apr 1, 2004.

[22] F. Grassi and S. A. Pignari, "Immunity to Conducted Noise of Data Transmission Along DC Power Lines Involving Twisted-Wire Pairs Above Ground," *Temc,* vol. 55, *(1),* pp. 195-207, 2013. Available: https://ieeexplore.ieee.org/document/6255785. DOI: 10.1109/TEMC.2012.2208117.

[23] H. Meng *et al*, "Modeling of transfer Characteristics for the broadband power line communication channel," *Tpwrd,* vol. 19, *(3),* pp. 1057-1064, 2004. Available: https://ieeexplore.ieee.org/document/1308327. DOI: 10.1109/TPWRD.2004.824430.

[24] A. Pinomaa, J. Ahola and A. Kosonen, "PLC Concept for LVDC Distribution Systems," *Com-M,* vol. 49, *(12),* pp. 55-63, 2011. Available: https://ieeexplore.ieee.org/document/6094006. DOI: 10.1109/MCOM.2011.6094006.

[25] A. G. Lazaropoulos and P. G. Cottis, "Broadband Transmission via Underground Medium-Voltage Power Lines-Part II: Capacity," *Tpwrd,* vol. 25, *(4),* pp. 2425-2434, 2010. Available: https://ieeexplore.ieee.org/document/5530341. DOI: 10.1109/TPWRD.2010.2052113.

[26] F. Aalamifar *et al*, "Modelling power line communication using network simulator-3," in Dec 2013, Available: https://ieeexplore.ieee.org/document/6831526. DOI: 10.1109/GLOCOM.2013.6831526.

[27] S. Robson, A. Haddad and H. Griffiths, "A New Methodology for Network Scale Simulation of Emerging Power Line Communication Standards," *Tpwrd,* vol. 33, *(3),* pp. 1025-1034, 2018. Available: https://ieeexplore.ieee.org/document/7564409. DOI: 10.1109/TPWRD.2016.2595639.

[28] S. Ramo, J. R. Whinnery and T. Van Duzer, *Fields and Waves in Communication Electronics.* (3rd ed.) New York: Wiley, 1994.

[29] D. M. Pozar, *Microwave Engineering.* (Fourth edition, international adaptation ed.) Hoboken, NJ: Wiley, 2021.

[30] S. Morsalin *et al*, "Diagnostic challenges in dielectric loss assessment and interpretation: a review," *IET Science, Measurement & Technology,* vol. 13, *(6),* pp. 767-782, 2019. Available: http://digital-library.theiet.org/content/journals/10.1049/iet-smt.2018.5597. DOI: 10.1049/iet-smt.2018.5597.

[31] B. Gustavsen, J. A. Martinez and D. Durbak, "Parameter determination for modeling system transients-Part II: Insulated cables," *Tpwrd,* vol. 20, *(3),* pp. 2045-2050, 2005. Available: https://ieeexplore.ieee.org/document/1458878. DOI: 10.1109/TPWRD.2005.848774.

[32] David K. Knight. "Components and Materials: Part 6." G3YNH. http://g3ynh.info/zdocs/comps/part_6.html (accessed May 15, 2023).

[33 B. Sareni *et al*, "Effective dielectric constant of periodic composite materials," *Journal of Applied Physics,* vol. 80, *(3),* pp. 1688-1696, 1996. Available: https://hal.science/hal-00140682. DOI: 10.1063/1.362969.

[34] J. van der Merwe, H. C. Reader and J. H. Cloete, "S-parameter measurements yielding the characteristic matrices of multiconductor transmission lines," *Temc,* vol. 40, *(3),* pp. 249-256, 1998. Available: https://ieeexplore.ieee.org/document/709423. DOI: 10.1109/15.709423.

[35] devolo. "G3-PLC Modem 500k Downloads." devolo. https://www.devolo.global/support/download/download/g3-plc-modem-500k (accessed May 25, 2023)

[36] devolo. "dLAN Green PHY eval board II Downloads." devolo. https://www.devolo.global/support/download/download/dlan-green-phy-eval-board-ii (accessed May 25, 2023)

[37] *Broadband PLC Transformers,* Revision 1.3, devolo. [Online] Avaliable: https://www.codico.com/en/coupler-82977-ut11359 (accessed May 25, 2023)

[38] AWR Microwave Office. (2023). Cadence. Accessed: June 13, 2023. Available: https://www.cadence.com/en_US/home/company/cadence-academic-network/university-program.html.

[39] F. Caspers, RF engineering basic concepts: S-parameters. (2012, Winter). Accelerator Physics. Cornell University. Available: https://arxiv.org/abs/1201.2346. DOI: 10.48550/arxiv.1201.2346.

[40] Qualcomm Atheros Open Powerline Toolkit. (2023). Qualcomm. Accessed: June 13, 2023. Available: https://github.com/qca/open-plc-utils.

[41] W. Fan *et al*, "Mixed-mode S-parameter characterization of differential structures," in 2003, Available: https://ieeexplore.ieee.org/document/1271579. DOI: 10.1109/EPTC.2003.1271579.

[42] *E5061B ENA Vector Network Analyzer Data Sheet,* Keysight Technologies, 2023.

[43] M. Tlich, G. Avril and A. Zeddam, "Coherence bandwidth and its relationship with the RMS delay spread for PLC channels using measurements up to 100 MHz," in *Home Networking*. Boston, MA: Springer US, pp. 129-142.